

RICo: Rotate-Inpaint-Complete for Generalizable Scene Reconstruction

Isaac Kasahara, Shubham Agrawal, Selim Engin, Nikhil Chavan-Dafle, Shuran Song, and Volkan Isler
Samsung AI Center, New York

Abstract

General scene reconstruction refers to the task of estimating the full 3D geometry and texture of a scene containing previously unseen objects. In many practical applications such as AR/VR, autonomous navigation, and robotics, only a single view of the scene may be available, making the scene reconstruction a very challenging task. In this paper, we present a method for scene reconstruction by structurally breaking the problem into two steps: rendering novel views via inpainting and 2D to 3D scene lifting. Specifically, we leverage the generalization capability of large language models (DALL-E 2) to inpaint the missing areas of scene color images rendered from different views. Next, we lift these inpainted images to 3D by predicting normals of the inpainted image and solving for the missing depth values. By predicting for normals instead of depth directly, our method allows for robustness to changes in depth distributions and scale. With rigorous quantitative evaluation, we show that our method outperforms multiple baselines while providing generalization to novel objects and scenes.

1. Introduction

The understanding of 3D scene geometry is essential for many down-stream applications. In robotics, it allows for accurate manipulation and motion planning considering the surrounding environment. In the field of augmented reality, it allows for better mapping and rendering to bridge the virtual world to the real world. With smartphones and robots that are equipped with high quality depth sensors, the task of 3D scene reconstruction is becoming feasible in these domains. These depth sensors allow for accurate reconstruction of the observed parts of the scene. However, to reconstruct the unseen parts, we must use prior information conditioned on the observed information. The missing information in the input image combined with the diversity in shapes, sizes, and depth distribution of the household objects presents a major challenge for scene reconstruction in-the-wild. In this paper, we study this problem in a general setting, where the goal is to reconstruct a complex scene with multiple novel objects, given only one RGB-D image

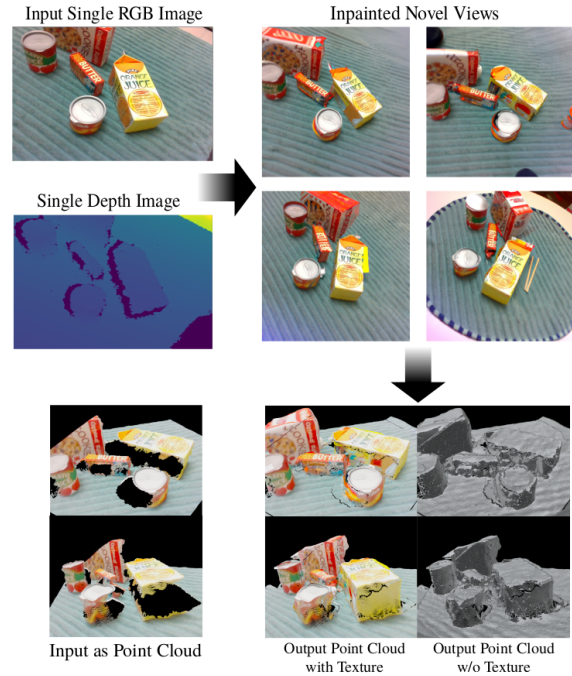


Figure 1: An example of 3D scene reconstruction from a single RGB-D image by generating inpainted novel views of the scene and lifting that information to 3D.

of the scene.

We present our method Rotate-Inpaint-Complete (RICo), which predicts both the 3D geometry and the texture of the unseen parts of the scene in the input image by leveraging the inpainting capabilities of large visual-language models. Given an RGB-D image of a scene, first we generate novel views (RGB and depth images) by rotating and then projecting the input scene. Then we use a surface-aware masking method to select regions in the image to allow us to inpaint utilizing the powerful 2D inpainting capabilities of DALL-E 2 [1] for exposing the potential object geometry not visible in the input image. Finally, we optimize the depth images using the input depth values and occlusion boundaries and normals estimated from the inpainted images. These inpainted and completed novel RGB-D views provide the reconstructed scene geometry as a fused pointcloud with associated textures. To

mitigate the object hallucination and spatial inconsistency of predictions from DALL-E 2, we integrate algorithmic features such as filtering inpainting outputs and enforcing consistency across viewpoints into our method that play a crucial role for generalizable, yet accurate and robust scene reconstruction.

We demonstrate our method on cluttered scenes with unseen household objects and categories. Through a series of rigorous quantitative experiments, we show that our approach outperforms baseline methods in settings where no training data is available.

In short, the contributions of this paper can be summarized as follows. *i)* We present an integrated approach for scene completion of unseen objects under occlusion and clutter, by solving the problem through novel view inpainting and 2D to 3D scene lifting. *ii)* We develop a method for selectively inpainting regions in the novel views of the input scene that enables synthesis of consistent 2D geometry. *iii)* We train a 2D to 3D lifting method on the YCB-V [2] dataset and demonstrate the generalization capability on novel household objects and categories which is crucial for maintaining the generalization capability of our integrated scene reconstruction method.

2. Related Work

2.1. Scene Reconstruction

Scene reconstruction refers to the problem of estimating the 3D geometry of an environment, usually containing multiple objects, from a single image. While object reconstruction, completing the 3D geometry of a single object, is well-studied, scene reconstruction is explored in limited settings. Previously, much of the work in scene completion focused on either room scales [3, 4], or in autonomous driving settings [5–7] where the scene geometries are usually more structured. In our paper, we focus on an object-level scale, specifically tabletop environments, where objects can be in cluttered configurations. While methods like Mesh R-CNN [8], CoReNet [9] and CenterSnap [10] show accurate reconstruction of objects at the scene level, they do not show generalization capabilities to objects in novel categories. Recently, [11] introduced a method for reconstructing 3D geometries of objects and scenes of unseen categories, and demonstrated strong generalization performance to objects in-the-wild. However, different from our setting, they mostly focus on isolated objects and scenes with little to no clutter. In contrast, our method can reconstruct geometries and textures of complex scenes with objects from novel categories under heavy occlusions, as we show in our experiments.

2.2. Inpainting

Inpainting is the process of filling in missing areas of images. Traditionally, inpainting methods made use of image priors such as self-similarity for tasks like image restoration, where gaps with missing or corrupt values to be filled are usually small holes. Deep learning methods, on the other hand, using large amounts of training data achieved remarkable success for inpainting images with semantically consistent contents. Generative adversarial networks [12], for example, were shown to handle many challenging inverse problems, including image denoising [13], super-resolution [14], and inpainting [15–17]. More recently, resulting from the growth of visual language diffusion models, inpainting through image diffusion has also taken off [1]. These models, having been trained on millions of images, have demonstrated their ability to generalize to many different objects, scenes, and styles. In this paper, we develop a process to use a visual language diffusion model for inpainting cluttered scenes involving heavy occlusions.

2.3. Text-to-3D Synthesis

Another area that is currently rapidly being explored is that of shape completion using visual-language models with a combination of neural radiance fields (NeRF) [18]. Papers such as [19–21] demonstrate the ability to generate 3D models of very diverse objects from merely a text description. While the objects these methods can render may appear very realistic, they are not grounded to any real world geometry, so may not be as useful when estimating the shape of real objects. To overcome this limitation, papers such as [22, 23] extend these methods to reconstruct based on a ground truth reference image. These papers demonstrate high accuracy on individual objects, but do not demonstrate the ability to reconstruct multiple objects in cluttered scenes. While runtime is a concern for these methods, as optimizing neural radiance fields can take up to an hour to produce realistic results, even newer methods attempt to produce faster results by optimization without NeRF [24]. While better optimized for speed, this method is still limited in focus to only single object reconstruction and does not directly generalize to the setting we study in this paper.

3. Method

In this section, we introduce our method Rotate-Inpaint-Complete, or RICO, to generate generalizable reconstructions of 3D scenes containing multiple objects, given a single RGB-D image of the scene.

RICO takes in as input an RGB-D image $\mathcal{I} = (\mathbf{I}, \mathbf{D}) \in \mathbb{R}^{H \times W \times 4}$ and outputs a color point cloud $S \in \mathbb{R}^{N \times (3+3)}$, where N is the number of predicted points in the scene. Our method consists of three main components: 1) An inpainting step that takes in an RGB-D image \mathcal{I} and outputs an in-

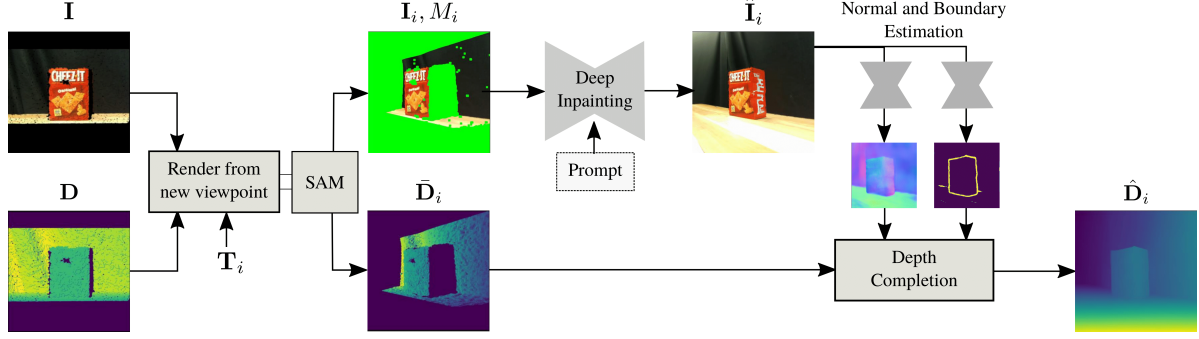


Figure 2: **Method Overview:** RICO takes as input an RGB-D image and starts by rendering incomplete RGB-D images $\bar{\mathbf{I}}_i$ and $\bar{\mathbf{D}}_i$ from a new viewpoint \mathbf{T}_i . The missing RGB values of $\bar{\mathbf{I}}_i$ are inpainted using a diffusion-based VLM given a generic prompt, such as “household objects on a table”, where the pixels to be inpainted are determined by our Surface-Aware Masking (SAM) technique. The inpainted image is used to predict surface normals and occlusion boundaries at the new viewpoint \mathbf{T}_i , which are then used for completing the missing depth values along with the incomplete depth image $\bar{\mathbf{D}}_i$. After repeating this process for n viewpoints, the final output of RICO is a merge of deprojected depth predictions.

1) A depth completion component that takes in the inpainted RGB image $\hat{\mathbf{I}}_i$ as well as an incomplete depth image $\bar{\mathbf{D}}_i$ rendered from the viewpoint \mathbf{T}_i , and outputs a completed depth $\hat{\mathbf{D}}_i$ at that viewpoint. 2) A depth completion component that takes in the inpainted RGB image $\hat{\mathbf{I}}_i$ as well as an incomplete depth image $\bar{\mathbf{D}}_i$ rendered from the viewpoint \mathbf{T}_i , and outputs a completed depth $\hat{\mathbf{D}}_i$ at that viewpoint. 3) An iterative method that utilizes the two other components to generate completed RGB-D images at rotated novel views and used them to reconstruct the scene. The following subsections will explain each of these components in detail.

3.1. Inpainting

This section describes the inpainting process, as well as the intermediate steps taken before and after to go from the input image \mathbf{I} to $\hat{\mathbf{I}}_i$ at a novel viewpoint \mathbf{T}_i .

3.1.1 Rotate and Project RGB-D Image

Given an RGB-D image of a scene and the camera intrinsics, we deproject the image into a point cloud in the camera frame. This point cloud is then rotated by an angle θ about its center point and rendered at the novel view following masking procedure, which we describe in detail in Section 3.1.2. The camera projection of the rotated point cloud creates a new RGB-D image $\bar{\mathbf{I}}_i$ with both missing RGB and depth information as seen in Figure 2. Small holes of the missing RGB values are filled with a naive inpainting algorithm [25].

3.1.2 Surface-Aware Masking

In order for inpainting to work properly, a mask covering the areas to inpaint needs to be generated. After rotating and projecting to the new camera frame, any 3D space possible to be reconstructed needs to be represented as inpainting

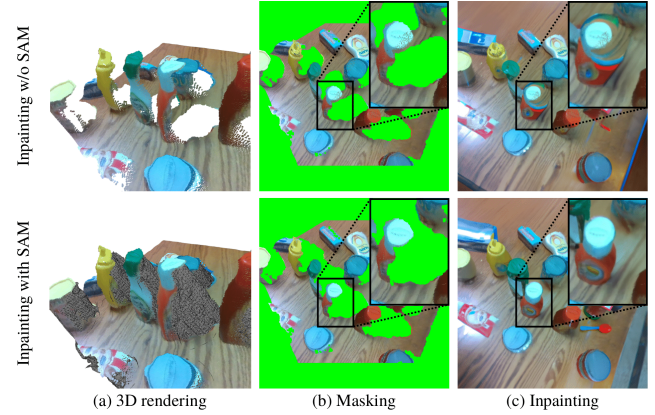


Figure 3: Surface-Aware Masking (SAM) is a necessary pre-processing step to obtain realistic inpaintings. Naively rotating the input point cloud moves the background pixels next to the foreground object pixels (b-top) which results in poor inpainting (c-top). Using SAM, we correctly mask out the background pixels which results in good inpainting results (b-bottom).

mask in the 2D image. To solve this problem, a 3D frustum is generated from the original camera and depth image. For every pixel in the original camera frame, a ray is cast from the camera through each point in the projected point cloud from \mathcal{I} . Once the ray has passed through its respective point, it is used to generate a list of points along the ray from that depth onward with equal spacing c . This is done for every ray, and from this process results a point cloud covering the potential space that the 3D scene could possibly fill. This point cloud is then converted to a mesh, and when the point cloud from the RGB-D image \mathcal{I} is rotated to novel views, the mesh is rotated with it. Finally, when projecting back to the camera frame after rotation, points

that are occluded by the mesh are discarded. Any blank pixels are then used as the 2D inpainting mask to be filled when passed to the inpainting step. This procedure of generating the final image and mask is detailed in Algorithm 1 and its outputs are shown in Figure 2, with the green pixels representing the inpainting mask. Figure 3 shows that our surface-aware masking is a crucial step for accurate image inpainting.

Algorithm 1 SURFACE-AWARE MASKING (SAM)

Require: Input RGB-D image $\mathcal{I} = (\mathbf{I}, \mathbf{D})$, intrinsics \mathbf{K} , new viewpoint \mathbf{T}_i
 $U \leftarrow$ Subsample pixels from a uniform grid in \mathcal{I}
 $X \leftarrow \{\}$ \triangleright initialize an empty point set.
for all $\mathbf{u} \in U$ **do**
 $\mathbf{x} \leftarrow \mathbf{D}(\mathbf{u})\mathbf{K}^{-1}\mathbf{u}$ \triangleright deprojection of \mathbf{u} to 3D point \mathbf{x} .
 for $i \leftarrow 1$ to m **do**
 $\mathbf{p} \leftarrow \mathbf{x} + i \cdot c \cdot \mathbf{K}^{-1}\mathbf{u}$
 $X \leftarrow X \cup \{\mathbf{p}\}$ \triangleright set of points with equal spacing.
 $\mathcal{M} \leftarrow \text{Mesh}(X)$ \triangleright surface triangulation to create a mesh.
 $\bar{\mathbf{I}}_i, \bar{\mathbf{D}}_i \leftarrow$ Reprojection of \mathbf{I}, \mathbf{D} in camera viewpoint \mathbf{T}_i , where missing values are set to 0.
 $\tilde{\mathbf{D}}_i \leftarrow$ Depth map rendering of \mathcal{M} in camera \mathbf{T}_i
 $M \leftarrow \mathbf{0}_{H \times W}$ \triangleright initialize the mask image as zeros.
for all $\mathbf{u} \in M$ **do**
 $M(\mathbf{u}) \leftarrow 1$ if $\bar{\mathbf{D}}_i(\mathbf{u}) = 0 \vee \bar{\mathbf{D}}_i(\mathbf{u}) > \tilde{\mathbf{D}}_i(\mathbf{u})$
return $M, \bar{\mathbf{D}}_i$

3.1.3 Diffusion-based Inpainting

Once these preprocessing steps have been completed, we pass the processed image and a mask of areas to be filled in to the inpainting algorithm. We use DALL·E 2 [1] for image inpainting since it demonstrates the ability to produce the most realistic results. This model takes in the incomplete image $\bar{\mathbf{I}}_i$, the mask generated in the previous step M , and an input prompt P that describes the context of the image in words. To demonstrate the generalizability of our method, all our scenes use the generic prompt “*household objects on a table*” when generating inpainted images, although we explore using more specific prompts in our ablation experiments (Section 4.6). The output from this inpainting method is an image $\hat{\mathbf{I}}_i$ that now contains estimated areas from the diffusion model. Figure 2 shows an example before and after inpainting with DALL·E 2.

3.1.4 Inpainting Ranking Step

The resulting images from the inpainting method may vary in terms of their perceived realism for every new generation. We use it to our advantage by generating multiple inpainted

images for the same incomplete image and mask. These inpainted images are then compared against the input prompt P by encoding them to the CLIP embedded space [26]. The image containing the highest similarity is chosen as the final inpainted image $\hat{\mathbf{I}}_i$ at viewpoint \mathbf{T}_i .

3.2. Depth Completion

This section describes the steps taken for generating a complete depth map $\hat{\mathbf{D}}_i$ from an incomplete depth image $\bar{\mathbf{D}}_i$ as well as its corresponding RGB image. For depth completion, we use a method proposed by Zhang et al. [27]. This method works by estimating the normals and occlusion boundaries from the RGB image, and then optimizes for the complete depth by utilizing the estimated normals, occlusion boundaries, and incomplete depth.

3.2.1 Normals and Occlusion Boundaries Prediction

In order to obtain estimations for the normals and occlusion boundaries, we train Deeplabv3+ with DRN-D-54 on ground truth normals, in the same manner as Sajjan et al. [28]. The ground truth normals are obtained using the depth images from the YCB-V training dataset [2], the YCB-V synthetic dataset [29, 30], and the HomebrewedDB synthetic dataset [31]. The occlusion boundaries are also obtained by using the ground truth depth from the same datasets, and trained in the same manner as [28].

3.2.2 Optimize for Depth

Given the incomplete depth, the estimated normals from the image, and estimated occlusion boundaries, we solve for the completed depth. The main idea behind this method in [27] is that the areas with missing depth can be computed by tracing along the estimated normals from areas of known depth with the occlusion boundaries acting as barriers where normals should not be traced across. Formally we solve a system of equations to minimize an error E , where E is defined as $E = \lambda_D E_D + \lambda_S E_S + \lambda_N E_N B$. Here, E_D is the distance between the ground truth and estimated depth, E_S influences nearby pixels to have similar depths, and E_N measures the consistency of estimated depth and estimated normal values. We use the same $\lambda_D, \lambda_S, \lambda_N$ values from Sajjan et al [28].

3.3. Scene Completion

This section describes the complete process we follow to reconstruct a 3D scene from a single RGB-D image.

3.3.1 Point Cloud Rotation

Our main method consists of first deprojecting the original RGB-D image into a point cloud. The original image will be referred to as \mathbf{I}_0 . Next, we rotate the point cloud

around its mean along the world z -axis (or perpendicular to the ground plane) by angle θ . The rotated point cloud is then projected back into the original camera plane. This results in an incomplete RGB image as well as an incomplete depth image. The RGB image is then inpainted, and used to complete the depth image as described in the depth completion section above. This new viewpoint can be seen in Figure 5 as T_1 . We denote the completed RGB-D image from this viewpoint as \hat{I}_1 . We then take the image I_0 , and repeat this process, this time rotating by angle $2 \times \theta$ to obtain viewpoint T_2 and image \hat{I}_2 . This whole process is repeated two more times with $-\theta$ and $2 \times -\theta$ as rotation values to obtain viewpoints T_3 and T_4 respectively. Resulting from these steps, we obtain four completed novel views of the scene $[\hat{I}_1, \hat{I}_2, \hat{I}_3, \hat{I}_4]$.

3.3.2 Enforcing Consistency Across Viewpoints

The final step in our method involves combining these generated viewpoints while enforcing consistency across them. One drawback of utilizing DALL-E 2 for inpainting real objects, is its inconsistent completion of objects as well as the creation of objects that are not originally in the scene. To combat this issue, we filter for consistent predictions across viewpoints. The final prediction is achieved by first deprojecting the RGB-D images \hat{I}_1 and \hat{I}_2 from viewpoint T_1 and T_2 respectively back into the world frame as point clouds. The intersection of these point clouds are taken, and this intersection of points is added to our final prediction. The same process is taken with images \hat{I}_3 and \hat{I}_4 from their viewpoints. With our final prediction being the point cloud from viewpoint T_0 , the intersection between point clouds from T_1 and T_2 , as well as T_3 and T_4 . By taking only the points that both views predict are there, we find that our final output point cloud of the completed scene S contains more accurate geometry and color.

4. Experiments

In this section, we evaluate the performance of our scene completion method on a single view RGB-D image and on the out-of-training distribution dataset. We also report ablation studies for understanding the dependence of our method on (1) prompt specificity, (2) viewpoint angles, and (3) consistency filtering.

4.1. Implementation Details

The inpainting step of our algorithm is based on OpenAI’s DALL-E 2 API. For our implementation of SAM, we choose a c value of 0.01 meters with $m = 100$ points. In our method, for choosing new viewpoints we use a θ value of 20° . For our consistency between viewpoints method, we choose a threshold of 0.01 meters when computing the intersection between points in the viewpoints point clouds.

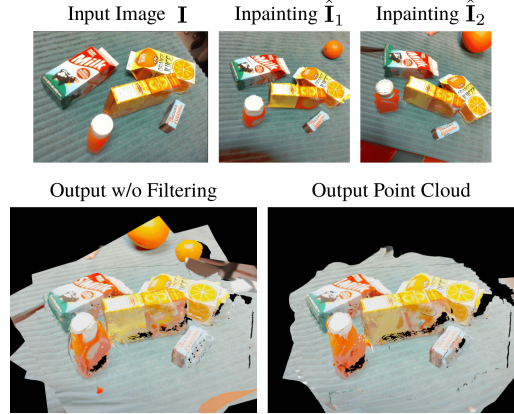


Figure 4: The consistency filtering step is necessary to remove hallucinated objects from inpainting. For example, the oranges in the top right of the images get filtered out.

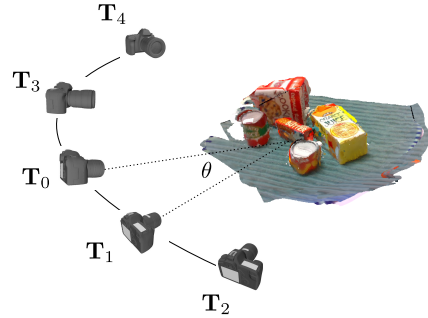


Figure 5: Our method synthesizes RGB-D images from novel viewpoints T_i , $i = 1 \dots 4$, with equal angle spacing θ for 3D reconstruction of the scene.

More information about our implementation can be found in our supplementary materials.

4.2. Datasets

We trained our depth completion model using the YCB-V training dataset [2]. For testing, we test on 8 unseen scenes from the YCB-V test set, and select 5 RGB-D images from each of the scenes, i.e., we test on a total of 40 RGB-D images total across 8 unseen scenes. For ground truth point clouds, and deproject the RGB-D frames of the scene and concatenate them together. We also place the ground truth meshes in the scene for the objects and convert those to point clouds before concatenating them as well. This creates a large point cloud covering the majority of the scene with full geometry of the objects in the scene.

To demonstrate our model’s capabilities of generalizing to unseen objects and to entirely new datasets, we also compare our method on the HOPE dataset [32]. HOPE test set only contains individual RGB-D images and is unusable for generating full scene point cloud. Instead, we use

HOPE training dataset for evaluation, as the train set contains RGB-D video and cluttered tabletop scenes with novel objects. The dataset has 10 scenes, and we again sample 5 frames per scene for a total of 50 RGB-D test images. Ground truth point clouds are obtained in the same manner as the YCB-V dataset.

4.3. Metrics

We evaluate our method on standard 3D reconstruction metrics, **Intersection-over-Union (IoU)**:

We voxelize the ground truth and predicted point clouds at a fixed resolution and compute the IoU score by dividing the number of voxels that intersect to that of their union. In our experiments, we evaluate all the methods at the same grid resolution of 100^3 after rescaling the predictions and ground truth to fit into the unit cube. **Chamfer Distance (CD)**: Chamfer distance is commonly used to measure the similarity between two point sets and is defined as:

$$CD(X, Y) = \frac{1}{|X|} \sum_{x \in X} \min_{y \in Y} \|x - y\|_2 \quad (1)$$

We separately report $CD(S, S^*)$ and $CD(S^*, S)$, as well as their their sum. $CD(S, S^*)$ measures how close the reconstructed points from S are to the ground truth points S^* , whereas $CD(S^*, S)$ computes how well the ground truth shape is covered. **F-Score**: Following [33], we also report F-Score@1% which is a measure for the percentage of the surface points that were reconstructed correctly.

4.4. Baselines

We compare our novel scene completion method against four baselines: **Convolutional Occupancy Networks (CON)** [34] is a 3D scene reconstruction method that inputs a sparse point cloud of a scene for reconstruction. We use the pretrained model for their *Synthetic Indoor Scene dataset* where similar to our YCBV and HOPE datasets, they place multiple ShapeNet [35] objects in indoor scenes. **CoReNet** [9] is a multi-object shape estimator that inputs an RGB image and estimates a mesh. We compare against CoReNet’s pretrained model qualitatively, as CoReNet’s predictions lack scale information. **ShellNet** [36] is a shape completion method trained on single objects. ShellNet inputs scene depth image and object instance mask and produces reconstruction for the object instance. We re-implemented ShellNet’s architecture and trained it with Mask R-CNN [37] as the segmentation network on YCB-V dataset. Finally, we compare against **CenterSnap** [10], a multi-object point cloud prediction method. CenterSnap inputs an RGB-D image and predicts point clouds for each object in the scene. Similar to CenterSnap’s original training method, we first train it on YCB-V synthetic dataset [29, 30], then fine-tune it on the YCB-V real training dataset [2]. Since CenterSnap and ShellNet only predict the point

Method	IoU \uparrow	F-Score \uparrow	$CD(S^*, S) \downarrow$	$CD(S, S^*) \downarrow$	$CD \downarrow$
YCB-V [2]					
CON [34]	0.15	0.399	0.102	0.027	0.129
ShellNet [36]	0.213	0.618	0.028	0.022	0.05
CenterSnap [10]	0.255	0.683	0.030	0.003	0.033
RICo (Ours)	0.284	0.688	0.025	0.011	0.036
HOPE [38]					
CON [34]	0.114	0.312	0.103	0.03	0.133
ShellNet [36]	0.181	0.547	0.04	0.03	0.07
CenterSnap [10]	0.211	0.617	0.046	0.004	0.050
RICo (Ours)	0.298	0.702	0.039	0.004	0.043

Table 1: Comparison of methods for the task of 3D scene completion on the YCB-V [2] and HOPE [38] datasets. Higher numbers for the IoU and F-score metrics, and lower numbers for the Chamfer Distances (CD) indicate better performance.

clouds for objects and not the rest of the scene, for a fair comparison, we concatenate the input RGB-D image deprojected point cloud to each of the outputs before evaluating.

4.5. Results

Table 1 shows quantitative evaluations on within-training-distribution YCB-V dataset [2] and out-of-training-distribution HOPE dataset [32]. On YCB-V dataset, RICo is able to outperform CON and ShellNet on all 3D scene reconstruction metrics. CON takes as input a sparse point-cloud of the scene. When major parts of the input point clouds are missing, as the common case for single-view RGB-D point clouds, CON fails to infer those regions. ShellNet is trained to predict back-side depth image for the detected object. We notice that with varying viewing directions, ShellNet backside depths are either too thin or too thick resulting in low performance. MaskRCNN’s failure to detect objects also directly contributed to lower performance for ShellNet. CenterSnap inputs RGB-D image and predicts object shapes via a three-step procedure: (a) detect objects in the image, for each detected object, (b) predict canonical frame point-cloud, and (c) camera frame pose and camera frame scale. This procedure allows CenterSnap to learn strong shape and pose priors for objects within training distribution. Moreover, supervision from ground-truth object poses allowed CenterSnap to perform well within train distribution. RICo which is trained without ground-truth object pose or shape supervision is able to perform comparatively with CenterSnap in the overall CD metric.

On out-of-distribution HOPE dataset, RICo is able to outperform all baselines. This shows that our normal and occlusion boundary based depth completion method generalizes well to unseen novel scenes. Figure 7 shows qualitative results for scene completion on the HOPE dataset.

As a byproduct, our method also produces novel views of unseen multi-object scenes from a single RGB-D im-

age. Figure 8 shows our method compared to the ground truth. We show that by combining our masking method with DALL-E 2’s inpainting capability, realistic novels views can be generated for multiple unseen objects.

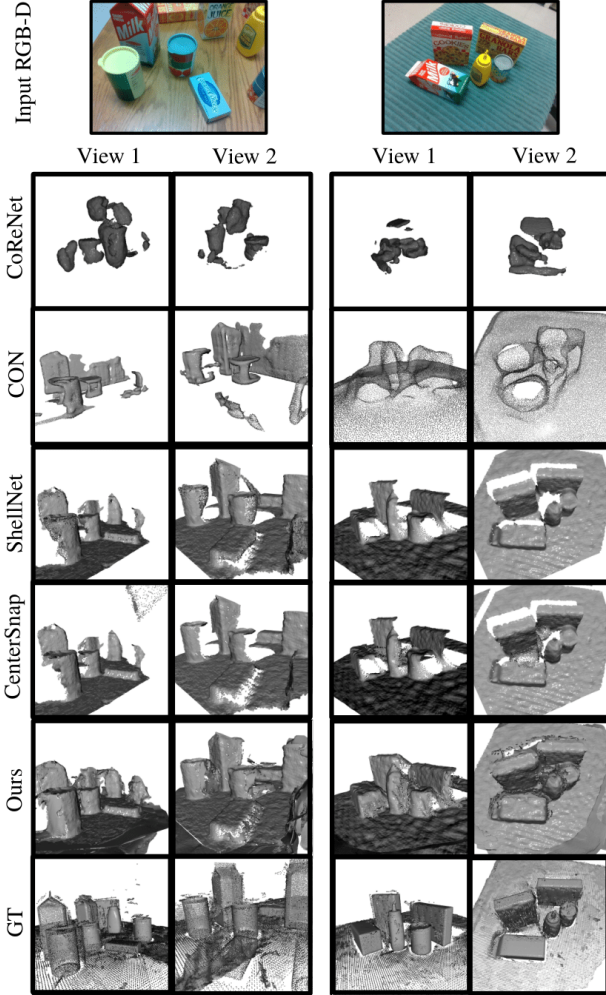


Figure 6: **Qualitative Comparison:** We compare our method against baselines for completing scene geometry given a single RGB-D image. View 1 and 2 show novel viewpoints of the predicted point clouds from each method.

4.6. Ablation Studies

Prompt Specificity: In our method, we used “household objects on a table” as a generic prompt for all scenes. To investigate whether the performance can be improved by using more specific prompts, we compare our method against a scene specific prompt. Specifically, for a scene containing n objects with object labels obj_i , we create the prompt as “a $obj_1, obj_2 \dots obj_{n-1}$, and obj_n on a table”. This list of objects is limited to the first 10 objects for larger scenes. We call this ablation RICO (S). Table 2 shows that

our method does not depend on specific prompt. While image diffusion models generally heavily depend on the input prompt for creating images, we hypothesize that our solution where we maximally retain the information present in the input RGB image, provides enough surrounding context and hence, does not need a very specific prompt.

Method	IoU \uparrow	F-Score \uparrow	CD \downarrow
RICO (S)	0.298	0.702	0.042
RICO	0.298	0.702	0.043

Table 2: Prompt specificity results on HOPE dataset [32]: RICO(S) denotes our model with scene specific prompt, as compared to RICO which inputs the general prompt - “household objects on a table” for all scenes.

Viewpoint Angles: Here, we ablate our method for different values for the angle of rotation between viewpoints θ (Section 3.3.1). We experimented with θ values of 10, 20, and 30 degrees and chose the best performing θ of 20 degrees as our final θ . Note that even with the larger θ of 30 degrees, our method’s performance does not change a lot.

Method	IoU \uparrow	F-Score \uparrow	CD(S^*, S) \downarrow	CD(S, S^*) \downarrow	CD \downarrow
RICO (10)	0.296	0.698	0.038	0.006	0.044
RICO (20)	0.298	0.702	0.039	0.004	0.043
RICO (30)	0.296	0.699	0.04	0.003	0.043

Table 3: Viewpoint angles study on the HOPE [38] dataset. 10, 20, and 30 denote the angle of rotation θ of the point cloud between inpainting steps as described in Section 3.3.1

Consistency Filtering: Table 4 shows results for our method without consistency filtering (Section 3.3.2). RICO (No Filter) has lower performance compared to RICO as DALL-E 2 does not produce consistent in-painting results across different views and often produce objects which are not in the scene. RICO with consistency filtering is able to aggregate coherent information from multiple inpainted views.

Method	IoU \uparrow	F-Score \uparrow	CD(S^*, S) \downarrow	CD(S, S^*) \downarrow	CD \downarrow
RICO (No Filter)	0.290	0.667	0.032	0.015	0.048
RICO (Ours)	0.298	0.702	0.039	0.004	0.043

Table 4: Consistency filtering results on the HOPE [38] dataset. RICO (No Filter) refers to reconstructions without any consistency filtering (Section 3.3.2).

Surface-Aware Masking: Figure 3 qualitatively reports the dependence of our method on Surface-Aware Masking step (Section 3.1.2). We observe that without SAM, the DALL-E 2’s inpainting algorithm confuses background in rotated point cloud as foreground and produces unrealistic artifacts.

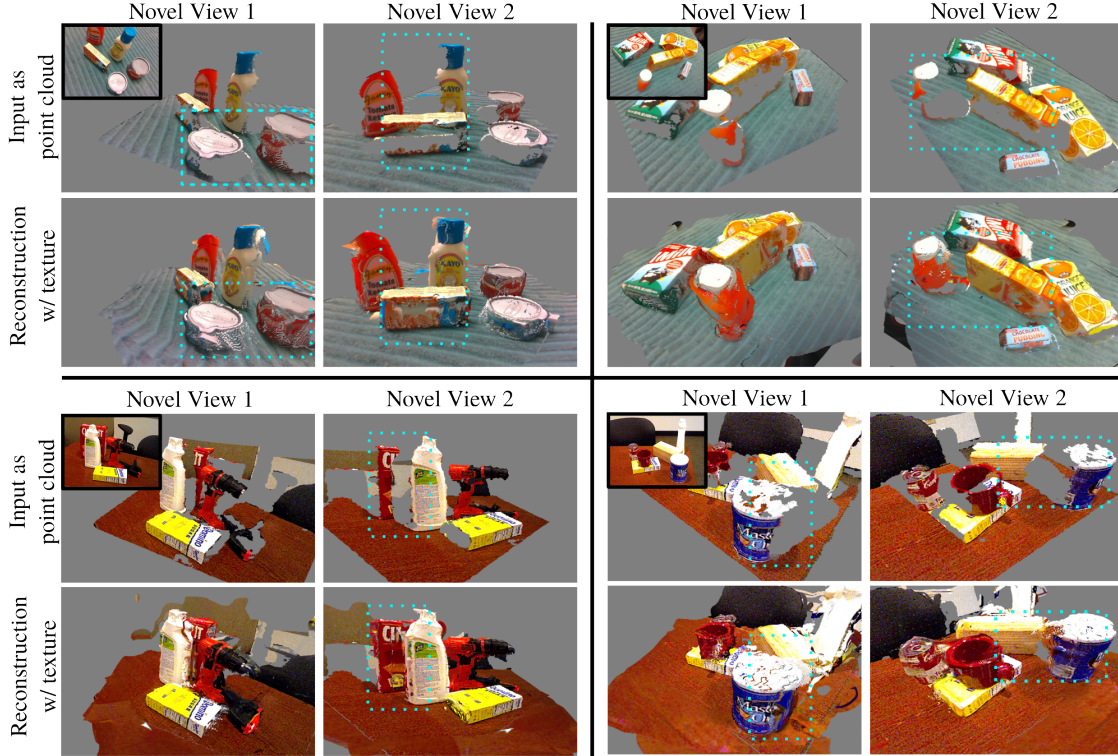


Figure 7: **Qualitative Results:** We show our scene completion results given a single RGB-D image, as color point clouds from two viewpoints. Top two rows are scenes from the HOPE dataset [38], and the bottom two are from YCB-V [2].

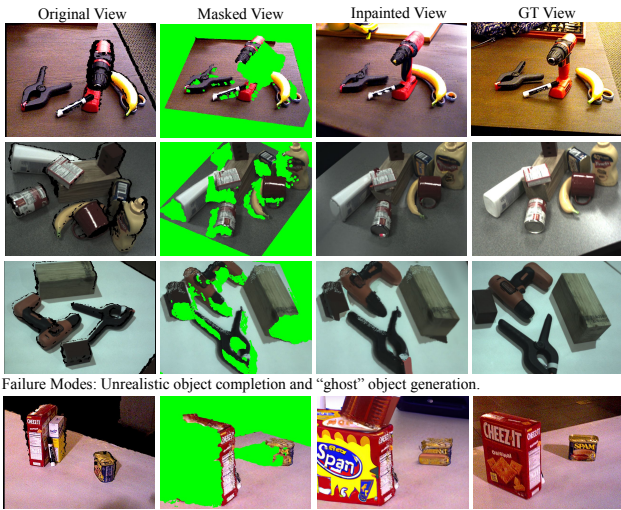


Figure 8: **Qualitative Novel View Results:** As a byproduct of our method we also show qualitative results for generating novel views of scenes with multiple objects on the YCB-V dataset.

5. Conclusion

We presented a novel 3D scene reconstruction method RICO. Our method solves the problem of 3D reconstruction of a cluttered scene of novel objects by leveraging the generalization capabilities of large visual language models. More specifically, our method utilizes the 2D inpainting capabilities of DALL-E 2, and generates a coherent set of inpainted views of the scene. It then lifts that information into 3D through a novel geometric multi-step method to finally output the point cloud of the reconstructed scene.

While we demonstrate the effectiveness of our method for generalizable scene completion, we also note that DALL-E 2 can generate unrealistic objects and parts of objects in the inpainted images. We mitigate this issue through various ways described in our method section, but these irregularities can adversely affect the reconstruction quality in a few cases (see Figure 8). While our method shows the ability to complete the front and sides of objects in our scene, the backside of objects is often left incomplete due to the limited angles of the viewpoints we use. At large angles away from the original viewpoint, the inpainting quality degrades due to the large areas of missing information which is an exciting yet challenging problem for future work.

References

- [1] Aditya Ramesh, Prafulla Dhariwal, Alex Nichol, Casey Chu, and Mark Chen. Hierarchical text-conditional image generation with clip latents. *arXiv preprint arXiv:2204.06125*, 2022. 1, 2, 4
- [2] Yu Xiang, Tanner Schmidt, Venkatraman Narayanan, and Dieter Fox. Posecnn: A convolutional neural network for 6d object pose estimation in cluttered scenes. In *Proceedings of Robotics: Science and Systems*, Pittsburgh, Pennsylvania, June 2018. 2, 4, 5, 6, 8
- [3] Shuran Song, Fisher Yu, Andy Zeng, Angel X Chang, Manolis Savva, and Thomas Funkhouser. Semantic scene completion from a single depth image. In *Proceedings of the IEEE/CVF Conference on Computer Vision and Pattern Recognition*, pages 1746–1754, 2017. 2
- [4] Angela Dai, Daniel Ritchie, Martin Bokeloh, Scott Reed, Jürgen Sturm, and Matthias Nießner. Scancomplete: Large-scale scene completion and semantic segmentation for 3d scans. In *Proceedings of the IEEE Conference on Computer Vision and Pattern Recognition*, pages 4578–4587, 2018. 2
- [5] Ran Cheng, Christopher Agia, Yuan Ren, Xinhai Li, and Liu Bingbing. S3cnet: A sparse semantic scene completion network for lidar point clouds. In *Conference on Robot Learning*, pages 2148–2161. PMLR, 2021. 2
- [6] Christoph B Rist, David Emmerichs, Markus Enzweiler, and Dariu M Gavrilă. Semantic scene completion using local deep implicit functions on lidar data. *IEEE transactions on pattern analysis and machine intelligence*, 44(10):7205–7218, 2021. 2
- [7] Anh-Quan Cao and Raoul de Charette. Monoscene: Monocular 3d semantic scene completion. In *Proceedings of the IEEE/CVF Conference on Computer Vision and Pattern Recognition*, pages 3991–4001, 2022. 2
- [8] Georgia Gkioxari, Jitendra Malik, and Justin Johnson. Mesh r-cnn. In *Proceedings of the IEEE/CVF International Conference on Computer Vision*, pages 9785–9795, 2019. 2
- [9] Stefan Popov, Pablo Bauszat, and Vittorio Ferrari. Corenet: Coherent 3d scene reconstruction from a single rgb image. In *Computer Vision—ECCV 2020: 16th European Conference, Glasgow, UK, August 23–28, 2020, Proceedings, Part II 16*, pages 366–383. Springer, 2020. 2, 6
- [10] Muhammad Zubair Irshad, Thomas Kollar, Michael Laskey, Kevin Stone, and Zsolt Kira. Centersnap: Single-shot multi-object 3d shape reconstruction and categorical 6d pose and size estimation. In *2022 International Conference on Robotics and Automation (ICRA)*, pages 10632–10640. IEEE, 2022. 2, 6
- [11] Chao-Yuan Wu, Justin Johnson, Jitendra Malik, Christoph Feichtenhofer, and Georgia Gkioxari. Multiview compressive coding for 3d reconstruction. *arXiv preprint arXiv:2301.08247*, 2023. 2
- [12] Ian Goodfellow, Jean Pouget-Abadie, Mehdi Mirza, Bing Xu, David Warde-Farley, Sherjil Ozair, Aaron Courville, and Yoshua Bengio. Generative adversarial networks. *Communications of the ACM*, 63(11):139–144, 2020. 2
- [13] Jingwen Chen, Jiawei Chen, Hongyang Chao, and Ming Yang. Image blind denoising with generative adversarial network based noise modeling. In *Proceedings of the IEEE Conference on Computer Vision and Pattern Recognition*, pages 3155–3164, 2018. 2
- [14] Christian Ledig, Lucas Theis, Ferenc Huszár, Jose Caballero, Andrew Cunningham, Alejandro Acosta, Andrew Aitken, Alykhan Tejani, Johannes Totz, Zehan Wang, et al. Photo-realistic single image super-resolution using a generative adversarial network. In *Proceedings of the IEEE Conference on Computer Vision and Pattern Recognition*, pages 4681–4690, 2017. 2
- [15] Deepak Pathak, Philipp Krahenbuhl, Jeff Donahue, Trevor Darrell, and Alexei A Efros. Context encoders: Feature learning by inpainting. In *Proceedings of the IEEE conference on computer vision and pattern recognition*, pages 2536–2544, 2016. 2
- [16] Satoshi Iizuka, Edgar Simo-Serra, and Hiroshi Ishikawa. Globally and locally consistent image completion. *ACM Transactions on Graphics (ToG)*, 36(4):1–14, 2017. 2
- [17] Shengyu Zhao, Jonathan Cui, Yilun Sheng, Yue Dong, Xiao Liang, Eric I Chang, and Yan Xu. Large scale image completion via co-modulated generative adversarial networks. *arXiv preprint arXiv:2103.10428*, 2021. 2
- [18] Ben Mildenhall, Pratul P Srinivasan, Matthew Tancik, Jonathan T Barron, Ravi Ramamoorthi, and Ren Ng. Nerf: Representing scenes as neural radiance fields for view synthesis. *Communications of the ACM*, 65(1):99–106, 2021. 2

- [19] Ajay Jain, Ben Mildenhall, Jonathan T Barron, Pieter Abbeel, and Ben Poole. Zero-shot text-guided object generation with dream fields. In *Proceedings of the IEEE/CVF Conference on Computer Vision and Pattern Recognition*, pages 867–876, 2022. 2
- [20] Ben Poole, Ajay Jain, Jonathan T Barron, and Ben Mildenhall. Dreamfusion: Text-to-3d using 2d diffusion. *arXiv preprint arXiv:2209.14988*, 2022. 2
- [21] Chen-Hsuan Lin, Jun Gao, Luming Tang, Towaki Takikawa, Xiaohui Zeng, Xun Huang, Karsten Kreis, Sanja Fidler, Ming-Yu Liu, and Tsung-Yi Lin. Magic3d: High-resolution text-to-3d content creation. *arXiv preprint arXiv:2211.10440*, 2022. 2
- [22] Dejia Xu, Yifan Jiang, Peihao Wang, Zhiwen Fan, Yi Wang, and Zhangyang Wang. Neurallift-360: Lifting an in-the-wild 2d photo to a 3d object with 360° views. *arXiv preprint arXiv:2211.16431*, 2022. 2
- [23] Luke Melas-Kyriazi, Christian Rupprecht, Iro Laina, and Andrea Vedaldi. Realfusion: 360° reconstruction of any object from a single image. *arXiv preprint arXiv:2302.10663*, 2023. 2
- [24] Alex Nichol, Heewoo Jun, Pratul Dhariwal, Pamela Mishkin, and Mark Chen. Point-e: A system for generating 3d point clouds from complex prompts. *arXiv preprint arXiv:2212.08751*, 2022. 2
- [25] Alexandru Telea. An image inpainting technique based on the fast marching method. *Journal of Graphics Tools*, 9(1):23–34, 2004. 3
- [26] Alec Radford, Jong Wook Kim, Chris Hallacy, Aditya Ramesh, Gabriel Goh, Sandhini Agarwal, Girish Sastry, Amanda Askell, Pamela Mishkin, Jack Clark, Gretchen Krueger, and Ilya Sutskever. Learning transferable visual models from natural language supervision. *CoRR*, abs/2103.00020, 2021. 4
- [27] Yinda Zhang and Thomas Funkhouser. Deep depth completion of a single rgb-d image. *The IEEE Conference on Computer Vision and Pattern Recognition (CVPR)*, 2018. 4
- [28] Shreeyak Sajjan, Matthew Moore, Mike Pan, Ganesh Nagaraja, Johnny Lee, Andy Zeng, and Shuran Song. Clear grasp: 3d shape estimation of transparent objects for manipulation. In *2020 IEEE International Conference on Robotics and Automation (ICRA)*, pages 3634–3642. IEEE, 2020. 4
- [29] Maximilian Denninger, Martin Sundermeyer, Dominik Winkelbauer, Dmitry Olefir, Tomas Hodan, Youssef Zidan, Mohamad Elbadrawy, Markus Knauer, Harinandan Katam, and Ahsan Lodhi. BlenderProc: reducing the reality gap with photorealistic rendering. *Robotics: Science and Systems (RSS) Workshops*, 2020. 4, 6
- [30] Tomáš Hodaň, Martin Sundermeyer, Bertram Drost, Yann Labbé, Eric Brachmann, Frank Michel, Carsten Rother, and Jiří Matas. BOP challenge 2020 on 6D object localization. *European Conference on Computer Vision Workshops (ECCVW)*, 2020. 4, 6
- [31] Roman Kaskman, Sergey Zakharov, Ivan Shugurov, and Slobodan Ilic. Homebreweddb: Rgb-d dataset for 6d pose estimation of 3d objects. In *Proceedings of the IEEE/CVF International Conference on Computer Vision Workshops*, 2019. 4
- [32] Stephen Tyree, Jonathan Tremblay, Thang To, Jia Cheng, Terry Mosier, Jeffrey Smith, and Stan Birchfield. 6-dof pose estimation of household objects for robotic manipulation: An accessible dataset and benchmark. In *International Conference on Intelligent Robots and Systems (IROS)*, 2022. 5, 6, 7
- [33] Maxim Tatarchenko, Stephan R Richter, René Ranftl, Zhuwen Li, Vladlen Koltun, and Thomas Brox. What do single-view 3d reconstruction networks learn? In *Proceedings of the IEEE/CVF Conference on Computer Vision and Pattern Recognition*, pages 3405–3414, 2019. 6
- [34] Songyou Peng, Michael Niemeyer, Lars Mescheder, Marc Pollefeys, and Andreas Geiger. Convolutional occupancy networks. In *Computer Vision—ECCV 2020: 16th European Conference, Glasgow, UK, August 23–28, 2020, Proceedings, Part III 16*, pages 523–540. Springer, 2020. 6
- [35] Angel X. Chang, Thomas Funkhouser, Leonidas Guibas, Pat Hanrahan, Qixing Huang, Zimo Li, Silvio Savarese, Manolis Savva, Shuran Song, Hao Su, Jianxiong Xiao, Li Yi, and Fisher Yu. ShapeNet: An Information-Rich 3D Model Repository. Technical Report arXiv:1512.03012 [cs.GR], Stanford University — Princeton University — Toyota Technological Institute at Chicago, 2015. 6
- [36] Nikhil Chavan-Dafle, Sergiy Popovych, Shubham Agrawal, Daniel D Lee, and Volkan Isler. Simultaneous object reconstruction and grasp prediction using a camera-centric object shell representation. In *2022 IEEE/RSJ International Conference on Intelligent Robots and Systems (IROS)*, pages 1396–1403. IEEE, 2022. 6

- [37] Kaiming He, Georgia Gkioxari, Piotr Dollár, and Ross B. Girshick. Mask R-CNN. *CoRR*, abs/1703.06870, 2017. 6
- [38] Yunzhi Lin, Jonathan Tremblay, Stephen Tyree, Patricio A. Vela, and Stan Birchfield. Multi-view fusion for multi-level robotic scene understanding. In *IEEE/RSJ International Conference on Intelligent Robots and Systems (IROS)*, pages 6817–6824, 2021. 6, 7, 8